

Affinity of hydroxyapatite (001) and (010) surfaces to formic and alendronic acids: a quantum-mechanical and infrared study†

Pieremanuele Canepa,^{ab} Fabio Chiatti,^a Marta Corno,^a Yuriy Sakhno,^a Gianmario Martra^a and Piero Ugliengo^{*a}

Received 11th July 2010, Accepted 7th October 2010

DOI: 10.1039/c0cp01143f

The affinity of the (001) and of the water reacted (010)WR hydroxyapatite surfaces towards formic and alendronic acids is studied with density functional theory (PBE functional) using periodic boundary conditions based on Gaussian basis set. Structures, energetic of the adsorption and vibrational features of the adsorbates are computed in order to understand at the atomic level both the cariogenic processes (for the formic acid) and the features of anti-osteoporosis drugs (for the alendronic acid). For both molecules the interaction energy is very high on an absolute scale, and for all examined cases, it is higher on the (010)WR HA surface than on the (001) one. For the latter, a number of cases by which the acidic proton of the adsorbate is transferred to the HA surface are also characterized. For the formic acid case, experimental infrared spectra are also measured and the position and nature of the C=O stretching bands have been found to be in excellent agreement with the quantum mechanical simulations. For alendronic acid IR experiments are still not available and the present predicted infrared spectra will be useful as a guide to interpret future experimental studies.

A. Introduction

Hydroxyapatite (HA), $\text{Ca}_{10}(\text{PO}_4)_6(\text{OH})_2$, is one of the most studied biomaterials, since it is the main component of tooth enamel and bone mineral phase. HA is commonly used in building biomedical devices with usage spanning from bone reconstruction to dental plants. HA has been extensively studied both experimentally^{1,2} and computationally^{3,4} to understand and characterize its macroscopic and chemical structure. The interactions of HA with some biological molecules, such as water and glycine, were also simulated,^{5–9} providing helpful interpretations and results comparable with experimental data. With this paper we want to give a new insight on the role of acids in HA dissolution and preservation.

Up to now, many studies attempted to comprehend the driving forces behind the cariogenic formation.^{10–19} Nevertheless, the huge number of factors implicated in this process (such as the bacterial flora, the bio-film, the organic acid blend) makes its understanding a puzzling but challenging task for scientists. It is well known that the enamel dissolution relies upon the presence of some organic acids, such as lactic, acetic, butyric, formic and citric acids, produced in the mouth as a by-product of the bacterial metabolism.^{10,13,15,16,19} Very little is known about the molecular process of the acid

demineralization of HA. Yoshida *et al.*, throughout XPS experiments, proposed a viable model of acid decalcification of HA:^{15,16} the carboxylic acid establishes weak interactions with the exposed Ca ions, whereas the acid proton is being released on the hydroxyl ion of the HA surfaces, forming water. Its release makes the adsorption stronger, with the possibility of calcium extraction. The above mechanism for the dissolution of HA is not addressed in this study as it will be the subject of future work. Here, we deal with adsorption surface phenomena limited either to physical adsorption or to simple proton transfer towards the HA surfaces from the molecular probes adopted in this study without exploring water release from the OH^- ions of the HA channels.

At the opposite side, a very active research field is the study of drugs which slow down the HA dissolution once interacting with its surfaces. The perturbation of the equilibrium between HA neo-deposition and re-absorption is characteristic of some metabolic bone disease, such as Paget's disease, osteoporosis, hyperparathyroidism and secondary osteolytic tumour.^{20–24} Among these drugs, medical scientists have recently employed bisphosphonates, because of their molecular compatibilities with the functionalities present at the HA surfaces.²³ In the present work we provide the atomistic details of the interaction between HA and one of the simplest administered acids, *i.e.* alendronic acid (AA). Many studies were conducted on its pharmacokinetic²⁵ and pharmacodynamics²⁶ but a few were meant to understand its molecular interactions with the bone mineral phase.^{27,28} Recent experimental studies highlighted the favourable interaction between HA and calcium alendronate throughout the synthesis of composite HA/AA nanocrystals but only one interaction geometry was proposed.^{29,30}

Here, the features of FA and AA adsorbed on the two most relevant HA surfaces, *i.e.* the (001) and the (010), are studied

^a Dipartimento di Chimica IFM, NIS Centre of Excellence and INSTM (Materials Science and Technology) National Consortium, UdR Torino, Via P. Giuria 7, Torino, Italy.

E-mail: piero.ugliengo@unito.it; Fax: +39 0112364596; Tel: +39 0116704596

^b School of Physical Sciences, Ingram Building, University of Kent, Canterbury, Kent, CT2 7NH, UK

† Electronic supplementary information (ESI) available: IR spectra of nanoHA before and after adsorption of FA. See DOI: 10.1039/c0cp01143f

with DFT (PBE functional) and Gaussian basis set as encoded in the CRYSTAL06 computer code.³¹ Structures and vibrational frequencies are discussed as well as the energetic of interaction. For the FA case, a through comparison between computed spectra and the experimental ones, recorded in our laboratory, will also be considered. As AA adsorption from the gas-phase is unfeasible, we only provide computed infrared spectra as a guideline for interpretation of future experiments.

B. Computational and experimental details

2.1 Computational

Hydroxyapatite (001) and (010)WR surfaces in interaction with formic and alendronic acids were simulated with the *ab initio* CRYSTAL06 code.³¹ The Hartree–Fock³² and the Kohn–Sham^{33,34} Hamiltonians are implemented in CRYSTAL06, for the study of periodic systems. CRYSTAL06 allows the geometry optimization as well as the calculation of the phonon frequencies at Γ point. MOLDRAW^{35,36} and VMD³⁷ were employed for manipulating and visualizing structures and electrostatic potential maps.

2.1.1 Basis set. The multi-electron wavefunction is described by linear combination of crystalline orbitals (CO) which, in turn, are expanded in terms of Gaussian-type basis set functions (GTO). In the present work, the first 10 electrons of hydroxyapatite (HA) calcium atoms were described with the Hay–Wadt small core pseudopotential ([HAYWSC]-31G). The exponent of the most diffuse shells is $\alpha_{\text{sp}} = 0.5 \text{ bohr}^{-2}$. A double split valence basis set of GTOs was employed for describing the remaining 10 electrons.³ A 85-21G(d) basis set was used for phosphorous atom with $\alpha_{\text{sp}} = 0.135 \text{ bohr}^{-2}$ for the most diffuse shell exponent and $\alpha_{\text{pol}} = 0.74583 \text{ bohr}^{-2}$ for polarization. Oxygen atoms were represented with a 6-31G(d) basis set with $\alpha_{\text{sp}} = 0.2742 \text{ bohr}^{-2}$ for the most diffuse shell exponent and $\alpha_{\text{pol}} = 0.538 \text{ bohr}^{-2}$ for polarization, while hydrogen atoms were described by 31G(p) basis set with $\alpha_{\text{sp}} = 0.1613 \text{ bohr}^{-2}$ for the most diffuse shell exponent and $\alpha_{\text{pol}} = 1.1 \text{ bohr}^{-2}$ for polarization. A 6-21G(d) basis set was applied in the description of carbon atom (with $\alpha_{\text{sp}} = 0.26 \text{ bohr}^{-2}$ for the most diffuse shell exponent and $\alpha_{\text{pol}} = 0.8 \text{ bohr}^{-2}$ for polarization) and nitrogen atom (with $\alpha_{\text{sp}} = 0.2832 \text{ bohr}^{-2}$ for the most diffuse shell exponent and $\alpha_{\text{pol}} = 0.8 \text{ bohr}^{-2}$ for polarization).³⁸ In order to check the accuracy of this basis set, we performed some calculations by improving the basis set for Ca with an all-electron (86-511G(d3)) where the most diffuse shell exponents are $\alpha_{\text{sp}} = 0.295 \text{ bohr}^{-2}$ and $\alpha_{\text{pol}} = 0.3191 \text{ bohr}^{-2}$ for polarization.³⁹ Both carbon and oxygen atoms were described with the Ahlrichs VTZ basis set.⁴⁰ Hydrogen and phosphorus basis sets were not changed.

2.1.2 Hamiltonian and phonon frequencies. All simulations were performed within the Density Functional Theory (DFT) framework using the Perdew–Burke–Ernzerhof (PBE).⁴¹ Recently, we have adopted the hybrid B3LYP functional to deal with HA material, both as such (bulk and surfaces) and when interacting with a variety of adsorbates (see Ref. 4 and

reference therein). We found a general good agreement between B3LYP results and experimental data. Here, we switched to the GGA PBE functional, as calculations are about three times quicker than the corresponding B3LYP ones, as this latter includes a fraction of the exact (and costly) Hartree–Fock exchange in the functional definition. This fact is important when modelling systems of larger size (larger supercell and adsorbates). Some comparison between PBE and B3LYP results will be performed for the case of AA adsorbed, to validate the PBE functional on the present systems.

Since in CRYSTAL06 the DFT exchange–correlation contribution is calculated by a numerical integration of the electron density, a pruned grid of 75 radial points was chosen along with one sub-interval with 974 angular points.

The Hamiltonian matrix was diagonalized over 10 k -points. Internal coordinate optimization was performed *via* an analytical gradient method, upgrading the numerical Hessian with the Broyden–Fletcher–Goldfarb–Shanno algorithm.^{42–45} We assumed that the interaction of a molecule with the slab structure does not affect the cell parameter values which were fixed to their bulk values.

Phonon frequencies calculations of adsorbed molecules (FA and AA) on HA surfaces were limited only to molecular fragments. This is fully justified by the large separation between the adsorbate vibrational modes and those involving the surfaces. For FA, surface oxygen atoms interacting with the acid and hydrogen atoms (deriving from water dissociation on the (010) surface) were also included in the fragment. Frequencies were calculated as the eigenvalues obtained by diagonalizing the mass-weighted Hessian matrix associated with the Γ point. The numerical Hessian matrix was computed by finite differences of the analytical gradient vector: the displacement for each atomic coordinate was set to $3 \times 10^{-3} \text{ \AA}$, reducing the convergence of the SCF cycle to 10^{-11} Hartree.

The remaining parameters such as thresholds for the integral selection, the integrated density, the threshold on the maximum force, the rms force, the maximum atomic displacement and the rms displacement were chosen as the default values.

2.1.3 Binding energy. In a periodic treatment of surface adsorption processes, the binding energy (BE) per unit cell is the net energy to remove the adsorbate from the surface to its gas phase, as below:

$$\text{BE} = E(\text{S//S}) + E_{\text{M}}(\text{M//M}) - E(\text{SM//SM})$$

where $E(\text{S//S})$ is the slab energy in its optimized geometry, $E_{\text{M}}(\text{M//M})$ is the molecular energy of the free adsorbate molecule in its optimized geometry and $E(\text{SM//SM})$ is the slab/adsorbate energy in its optimized geometry (the symbol following the double slash identifies the geometry at which the energy is computed). BE is a positive quantity for a bound adsorbate.

Two other significant contributions are the deformation energy of the slab (δE_{S}) and of the molecule (δE_{M}). Molecule deformation depends on both the lateral interactions between

adsorbates (ΔE_L) and its own geometrical deformation (ΔE_M), as seen below:

$$\delta E_S = E(S//SM) - E(S//S)$$

$$\delta E_M = E(M//SM) - E_M(M//M) = \Delta E_M + \Delta E_L$$

$$\Delta E_M = E_M(M//SM) - E_M(M//M)$$

$$\Delta E_L = E(M//SM) - E_M(M//SM)$$

ΔE_L can be either positive (repulsive) or negative (attractive).

Therefore, a binding energy free of deformation and lateral interactions terms can be defined as following:

$$\begin{aligned} BE^* &= BE + \delta E_S + \delta E_M \\ &= E(S//SM) + E(M//SM) - E(SM//SM) \end{aligned}$$

The BE value must be corrected for the basis set superposition error (BSSE), as we are employing localized Gaussian-type function basis set. The BSSE causes an overestimation of the BE. Here on, we adopted the widely accepted counter-poise correction for the BE* and the lateral interactions.⁴⁶

$$BE^{*C} = E(S[M]//SM) + E([S]M//SM) - E(SM//SM)$$

$$\Delta E_L^C = E(M//SM) - E_M(M[M]_n//SM)$$

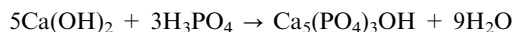
$$BE^C = BE^{*C} - \delta E_S - \Delta E_M - \Delta E_L^C$$

$$BSSE = BE - BE^C = BE^* - BE^{*C}$$

$E(S[M]//SM)$ and $E([S]M//SM)$ are the slab energies calculated including the ghost functions of the adsorbate layer and the HA slab, respectively. $E_M(M[M]_n//SM)$ is the energy of a single molecule in the adsorbate geometry in which the first neighbour replicas were ghosted.

2.2 Experimental

2.2.1 Materials. HA nanoparticles were kindly provided by the Prof. Roveri research group at the University of Bologna, where they were prepared by dropping a solution of H_3PO_4 (1.26 M, 0.6 L) into a $Ca(OH)_2$ suspension (1.35 M, 1.0 L), to accomplish the following reaction:



The reaction mixture was stirred under N_2 atmosphere for 24 h at 368 K. The stirring was then suspended and the mixtures were left standing for 2 h to allow for deposition of the inorganic phase. The HA powders were then isolated by filtration of the mother liquor, repeatedly washed with water and dried at room temperature.

Formic acid used as a source of vapour to be admitted onto the HA sample was from Sigma-Aldrich (98–100% purity). An aliquot was dropped in a reservoir and then degassed by several freeze–pump–thaw cycles.

2.2.1 Method. IR spectra were recorded by using a Bruker 88 spectrometer, equipped with a MCT detector, at a resolution

of 4 cm^{-1} and accumulating 150 interferograms for each spectrum.

To manage the interaction between hydroxyapatite and FA vapour in a controlled way, the HA powder was pressed in self-supporting pellets and then placed in quartz cells equipped with CaF_2 windows, designed to carry out spectroscopic measurements in the transmission mode. The cell was then connected to a conventional vacuum line (residual pressure: 1×10^{-5} mbar, 1 mbar = 10^2 Pa) allowing the thermal treatment and FA adsorption–desorption experiments to be carried out *in situ*. More simply, to collect the spectrum of liquid formic acid, a drop of FA was squeezed between two CaF_2 windows to form a thin film.

The spectra of adsorbed FA have been reported in absorbance, after subtraction of the spectrum of the HA pellet before the exposure to the acid vapour as a background. Resolution of sub-bands present in complex spectral profiles was achieved by using the “Curve fit” utility of OPUS 5.0 (Bruker Optic GmbH). A Gaussian shape was adopted for the components, and the fit was optimized by using a local least squared method.

Whereas FA is liquid at room T (saturated vapour pressure of 33.5 Torr),⁴⁷ alendronic acid is a solid phase at room T and its saturated vapour pressure is negligible. This hinders the feasibility of performing chemical vapour deposition of AA on the HA sample, as done for the FA case. Alternatively, the adsorption could be performed by dissolving AA in water. In this case, the quantum-mechanical simulation would require molecular dynamics to describe properly solvation/desolvation processes occurring during the AA adsorption, a task out of reach with our present facilities.

C. Results and discussion

In this section we present a brief description of the main geometrical features of FA and AA along with the most important surface sites of the HA (001) and the (010) surfaces. Geometrical features are essential together with electronic features to establish electrostatic complementarities between the HA surfaces and the adsorbate.

The PBE optimized FA geometry (Fig. 1) agrees reasonably well with previous experimental and theoretical studies.^{48–54}

As expected, the FA electron iso-density surface color-coded with the electrostatic potential⁵⁵ (hereon IDEP) shows clumps of positive values around the hydrogen atom of the OH group (blue zone), whereas the negative one (red zones) is mostly located near the carbonyl oxygen.

AA belongs to the geminal bisphosphonate category. It exhibits two phosphonic groups and one alcoholic substituent bound at the same carbon atom and a primary amino group linked to the γ -carbon of the alkyl chain. The acidic groups generate a negative potential whereas the positive potential is located around the terminal amino group. The alkyl chain remains relatively neutral, due to its apolarity.

In this study, two surfaces of hydroxyapatite were considered: the (001) and the (010). These ones were modeled, within the slab approach, starting from the fully optimized PBE HA bulk. Possible surface structural defects (position defects, steps, kinks, *etc.*) or substitutional defects

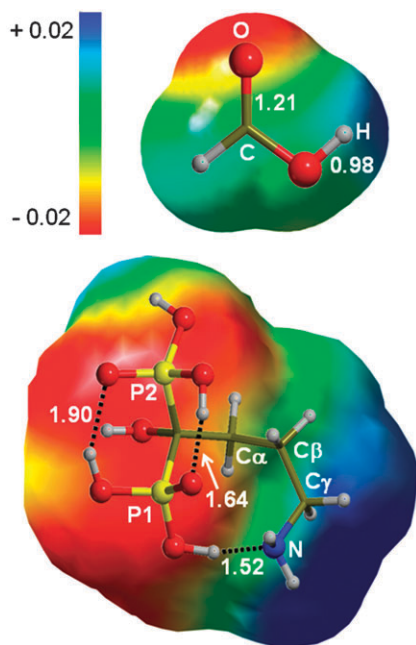


Fig. 1 Optimized geometries of FA and AA (bond distances, Å) superimposed with the electron iso-density surface color-coded with the electrostatic potential IDEP (isodensity 10^{-6} electrons, electrostatic potential between -0.02 and $+0.02$ Hartree).

(CO_3^{2-} , Na^+ , F^- , etc.) were not taken into account. For the (010), we chose to work with the water-reacted form of the surface (hereafter (010)WR) for two reasons: (i) the exoergonic dissociative chemisorptions of one water molecule onto the HA (010) surface (not observed for the (001) surface)⁵ and (ii) the ubiquitous presence of water in biological environments.

Table 1 shows the most important parameters characterizing the (001) and the (010)WR HA surfaces. Good agreement was found for the present PBE data when compared with previous B3LYP ones.^{5,56} The PBE HA (001) surface energy (E_{surf}) also agrees with other values found in the literature. Rulis *et al.*, by using the PBE functional and plane waves basis set (VASP, PBE, $E_{\text{cutoff}} = 600$ eV), found a value of E_{surf} of 0.871 J m^{-2} .⁵⁷ Filgueiras *et al.*,⁵⁸ with molecular dynamic (MD) techniques (METADISE), calculated two E_{surf} , 1.08 J m^{-2} and 1.12 J m^{-2} , since two feasible terminations were considered. MD simulations (DL_POLY) of Rabone and de Leeuw found a lower E_{surf} value, about 0.80 J m^{-2} , as they took into account temperature effects.¹⁷ In Fig. 2, the structures of the (001) and (010)WR are superimposed on their IDEP maps. A 3D view of the same structures is available as Fig. S2 of the ESI.† The chemical nature of surface sites is predictable when IDEP maps come to the rescue. Two varieties of site can be identified as

Table 1 PBE lattice parameters a , b and γ (Å and degrees), slab thickness T (Å), unit cell surface area A (Å²), surface energy E_{surf} (J m^{-2}) and average geometrical distances (Å) for the hexagonal HA (001) and (010)WR surfaces. The slab thickness is defined as the perpendicular distance between the most exposed Ca surface ions

PBE	a	b	γ	T	A	E_{surf}	P-O	Ca-O	O-H
(001)	9.297	9.297	120.0	13.3	74.8	1.03	1.564	2.384	0.978
(010)WR	6.932	9.227	89.97	13.3	63.9	/	1.600	2.390	0.976

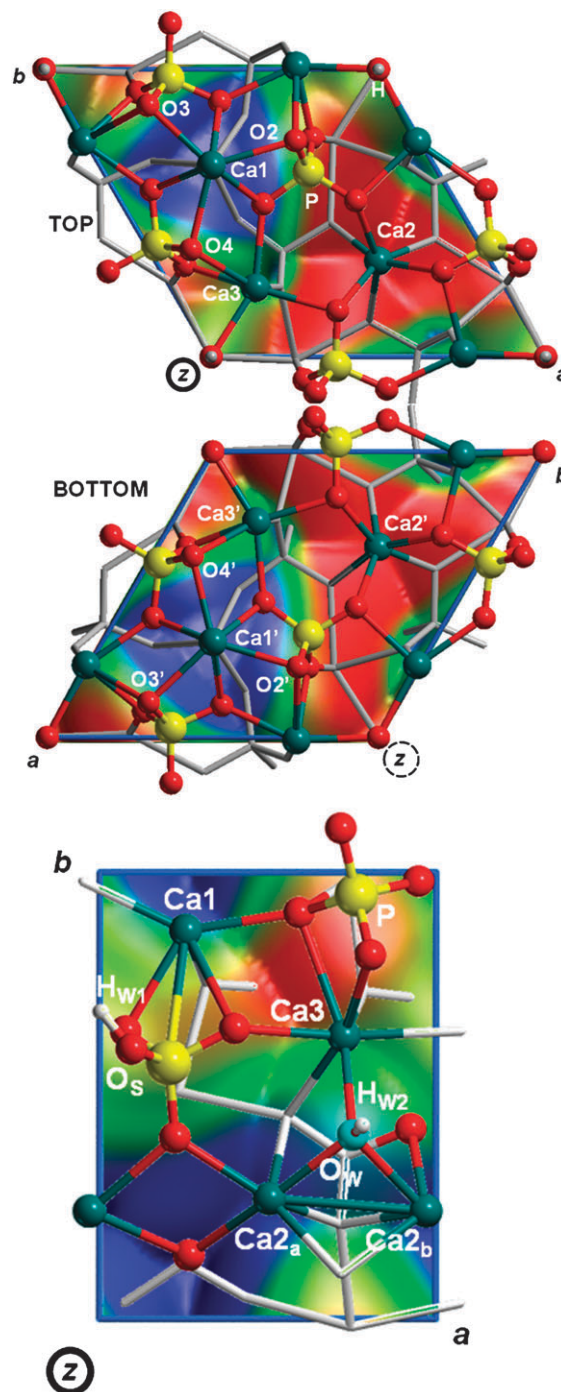


Fig. 2 Top view of hydroxyapatite (001) and (010)WR surfaces, superimposed with the IDEP (isodensity 10^{-6} electrons, electrostatic potential between -0.02 and $+0.02$ Hartree).

long as their Lewis acidity/basicity: (i) acidic sites, represented by Ca ions (blue zones), (ii) basic sites represented by the phosphate ions (red zones).

Chemical activity of each site is also influenced by their different exposure at the surface. In Fig. 2a and b, the order of exposure of Ca ions in the (001) slab is Ca1, Ca2 and Ca3 (and, similarly, their correspondent primes-labeled ions on the lower face of the slab). The chemical environment of Ca1 (and Ca1') in the (001) slab of HA is particularly interesting: three oxygen

atoms, equivalent by symmetry, form a triangle (here labeled as O2, O3 and O4) well highlighted in the IDEP. The two slab faces of the (001) behave differently because of the intrinsic dipolarity, due to the hydroxyl ions piled up through the surface.³ The electric dipole slightly polarizes positively the upper face and negatively the lower one, addressing to dissimilar adsorption effect.⁵⁹ No polarization is observed in the (010)WR as the hydroxyl ion pillars run along the *a* direction, *i.e.* perpendicular to the slab definition.³

As for the (010)WR surface, three types of Ca ions are well distinguished (see Fig. 2b): Ca1, Ca2 (*a*, *b*) and Ca3 ions. These latest ones were found as the most reactive in the (010) surface of HA,⁵ but their reactivity is reduced in the (010)WR surface because of the presence of the hydroxyl group originated from water dissociation (the atoms derived from the water dissociation are labelled as O_w, H_{w1} and H_{w2} in Fig. 2b).

3.1 Structure and energetic

Aiming to understand how FA and AA interact with HA, we present some models of adsorption on the (001) and (010)WR surfaces of HA using the principle of electrostatic complementarity. This principle has been successfully evoked to rationalize gas-phase adducts^{60,61} or host-guest interactions in molecular recognition⁶² and it is straightforwardly extended here to predict the best matching between adsorbant surface and adsorbate electric features before doing any real calculation of their interaction. Recent examples are found in Ref. 4.

3.1.1 FA in interaction with HA surfaces

Interaction with the (001) surface. FA was initially adsorbed with its oxygen atom on the Ca1 ion (the most exposed one, model FA_O4) with its acidic hydrogen (H_{FA}) pointing towards one of the near oxygen atoms (O4, in Fig. 3). After the optimization, the acidic proton (H_{FA}) remains shared between the oxygen atoms (O_{FA}-H_{FA} 1.19 Å, O4-H_{FA} 1.24 Å) and Ca1 interacts with a FA oxygen atom (Ca1-O_{FA} 2.29 Å).

As O2, O3 and O4 are symmetry related, we found similar adsorption geometries and energies, when the acid proton of FA is sequentially adsorbed either on O3 (FA_O3) or on O2 (FA_O2). The common BE is about 207 kJ mol⁻¹ (see Table 2), high enough to classify these processes as real chemisorptions. In a nutshell, the HA surface is undergoing a neutralization of its positive and negative charged sites mediated by FA molecules.

FA was also adsorbed on the Ca1' (corresponding to Ca1 on the lower face) to understand how the ferroelectricity, through the slab, affects its adsorption process (model FA_O3', Table 2). Since the electrostatic potential is more negative on the lower face of this surface, a more favorable interaction with the adsorbate would be expected. The BE gains only 13 kJ mol⁻¹ with FA_O3' exhibiting a very similar geometry compared with FA_O3 and the proton still shared between the involved oxygen atoms. The energies requested to deform the molecule (δE_M) from its gas-phase conformation span between 70 and 100 kJ mol⁻¹ (see Table 2), whereas the surface deformation contributions (δE_S) are about 10 kJ mol⁻¹ lower.

We also adsorbed FA on the sunken Ca3 (FA_Ca3, see Table 2), attempting to show how the exposure of a surface site can influence the interaction energy of the adsorbate-surface

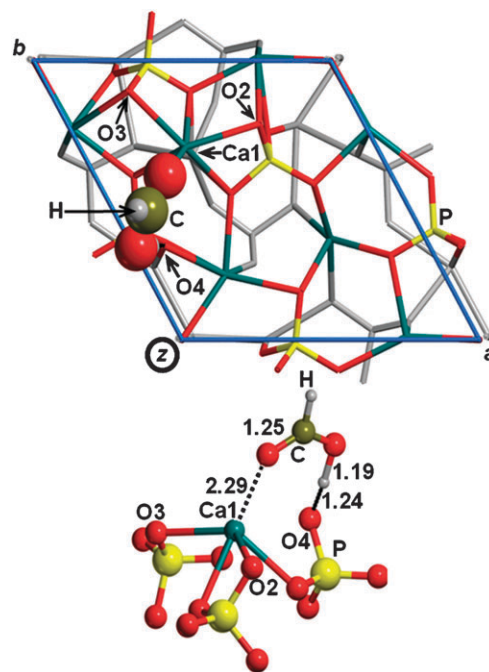


Fig. 3 FA on the HA (001) surface: top and local view of FA_O4 model. Bond lengths in Å. H-bonds Ca-O_s as dashed lines.

Table 2 PBE binding energies (kJ mol⁻¹) BE and their different energy contributions for FA interacting with the HA (001) surface: BE^C is the BE corrected for the BSSE; BE* is the BE free of the deformation contributions, BE*^C is the BSSE corrected BE*, δE_S and δE_M are deformation energies for the surface and the molecule, respectively

(001) model	BE	BE ^C	BE*	BE* ^C	δE_S	δE_M
FA_O4	207	156	312	261	29	76
FA_O4'	220	169	357	306	38	99
FA_Ca3	166	93	236	162	38	32
FA_Ca1,Ca3	172	—	—	—	—	—

adduct. The acid proton of FA does not appear close to the surface oxygen atoms as in the previous models (H_{FA}-O_s 1.42 Å). The BE value of only 166 kJ mol⁻¹ confirms the weak acidic character of the sunken Ca3 site in agreement with smaller FA geometrical deformation compared to FA_O3. In the latter model the oxygen atoms of FA were let interacting with Ca1 and Ca3 ions (model FA_Ca1, Ca3, see Table 2 and Fig. 4). The hydrogen atom, formerly belonging to FA, undergoes a complete dissociation becoming attached to the surface (O_s-H_{FA} 1.04 Å), with the formation of a short H-bond (H_{FA}...O_{FA} 1.53 Å, Fig. 4). The two oxygen atoms of the formate interact with two separate Ca ions (O-Ca1 2.32 Å and O-Ca1 2.37 Å, Fig. 4) and formate behaves as a bidentate ligand. The BE calculated for this model is 172 kJ mol⁻¹, which falls below those discussed previously for FA_O3 and FA_O3' and in line with that for FA_Ca3.

As the proton dissociation could be an artifact of the functional used,⁶³ we re-optimized this model with several other functionals, such as BLYP, PW91 and the hybrid B3LYP, ensuring that FA loses its acid proton in each case. Furthermore, we also checked for the basis set quality by running a single energy point calculation with the all-electron basis set described in the Computational details. The resulting

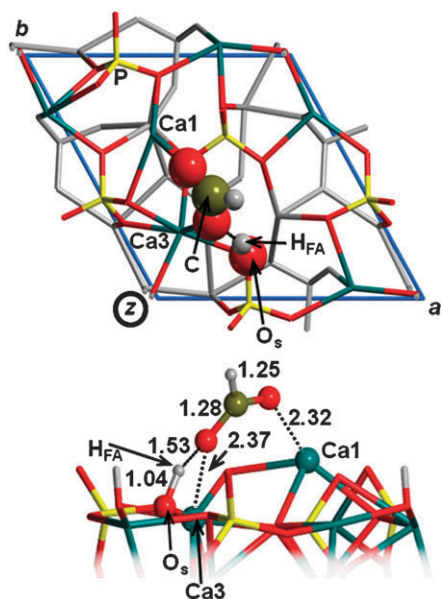


Fig. 4 FA on the HA (001) surface: top and local views of FA_Ca1,Ca3 model. Bond lengths in Å. H-bonds Ca–O_S as dashed lines.

BE of 176 kJ mol^{-1} agrees with the value of Table 2 computed with the standard basis set, indicating that for such interactions the default basis set provides robust results.

The BSSE estimated for all these simulations affects the BE within a 23%. When the deformation of both molecule and surface are taken into account, the resulting BE* and BE*^C (corrected for the BSSE) increase of 100–120 kJ mol^{-1} (see Table 2). Lateral interactions (FA/FA) were not taken into account in calculating δE_M , since the HA (001) unit cell is large enough to ensure a negligible interaction between the adsorbed FA molecules. Clearly, deformation and BSSE terms were not calculated for the FA_Ca1,Ca3 models as the dissociative process does not allow their definition.

Interaction with the (010)WR surface. A unique model of FA adsorbed on the (010)WR was considered (see Fig. 5). Our previous calculations⁵ had shown that water reacts spontaneously with the pristine (010) HA surface forming two new functionalities, namely POH and CaOH. As the morphology of the HA (010)WR surface is rather crowded due to the new groups, FA was initially adsorbed on Ca1 and Ca2_a (model FA_(010)). The acid hydrogen was orientated towards a surface oxygen (O_S). During geometry optimization, FA spontaneously dissociates ($H_{FA}-O_S$ 0.99 Å). The oxygen atoms of formate were involved in two types of interactions: (i) one oxygen was shared between two Ca2 (O–Ca2_a and O–Ca2_b, 2.44 Å), (ii) the other one interacted with the Ca1 ion (O–Ca1 2.42 Å). As a result, formate is bonded at three Ca ions of the surface.

The presence of the hydroxyl ions on the surface stabilizes both the dissociated proton and formate, as the acid proton forms a hydrogen bond with a surface oxygen ($H_{FA}\cdots O_S$ 2.02 Å). Formate oxygen interacting with Ca1 is also hydrogen bound with the nearby hydrogen atom H_{W2}, outcome of previous water dissociation on the initial (010) surface of HA. The reactivity of this surface, which was formerly found to be larger than the (001), is

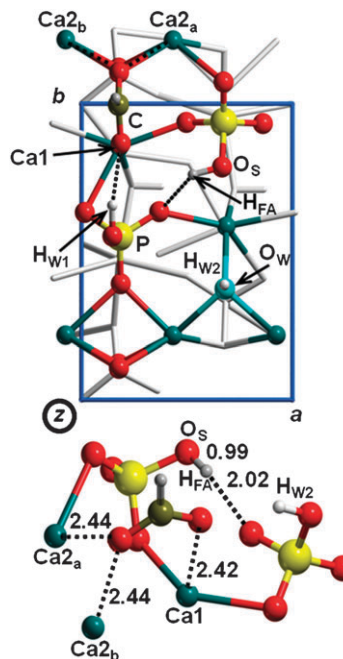


Fig. 5 FA on the HA (010)WR surface: top and local views of the FA_(010) model. Bond lengths in Å. H-bonds Ca–O_S as dashed lines.

here confirmed.^{5,56} Although the computed BE is very high (252 kJ mol^{-1}), we cannot determine the other contributions to the BE, due to FA dissociation.

The binding energies coming from these models are in agreement with other similar calculations where citric acid was adsorbed on the same HA surfaces.⁵⁸ However, as the adopted methodology was restricted to classical molecular mechanics, a one by one comparison with our energetic data is not straightforward. Nevertheless, the larger reactivity of the HA (010) surface with respect to the (001) resulted from the much larger interaction energy of the former compared to the latter, in agreement with the present PBE results. Furthermore, citric acid interacts similarly as FA through its carboxylic group with the topmost Ca ions.

3.1.2 AA in interaction with HA surfaces. AA structure was optimized starting from the coordinates obtained from an X-ray diffraction experiment on its calcium salt monocrystal,⁶⁴ by neutralizing the conjugate anion with the addition of a proton to the dissociated phosphonate group. The potential energy surface (PES) of AA results rather complex, because of the large number of degrees of freedom. We only explored a subset of zwitterionic as well as neutral (without separation of charges) gas phase conformers. Fig. 1 presents the structure of the most stable one, which contains three peculiar *intra*-molecular H-bonds. This conformation was not considered for the docking, as the molecule should unfold to maximize its electrostatic complementarity with the surface, a process which requires some extra energy. The interaction of the phosphonic groups was addressed towards the most exposed calcium ions on the surface, leaving the lighter and more movable amino group free to interact with a phosphate ion of the surface. The amino group can also set up strong interactions with a phosphonic group of an AA image, lying in adjacent cells.

Interaction with the (001) surface. Three cases of AA adsorbed on the (001) surface were simulated (Fig. 6). Fig. 6a shows the first model of neutral AA in which a phosphonic group transfers one of its acidic protons to the HA surface giving rise to a short H-bond (1.52 Å). A P=O group interacts with the most exposed Ca1 ion (Ca1–O 2.31 Å) of the HA surface while a H-bond is established between one OH group and the NH₂ group of a replicated AA molecule in a close cell (H···N 1.67 Å). The remaining phosphonic functionalities give rise to both *intra*-molecular H-bonds (1.68 Å and 1.84 Å) and interactions towards the HA surface (1.52 Å). For this structure the computed BE is 336 kJ mol⁻¹.

Fig. 6b envisages adsorption of AA in which a proton transfer occurred between a phosphonic group of one AA and the NH₂ group of a replicated AA molecule in a close cell (H···O 1.50 Å). The Ca1 engages two interactions with the P=O of the deprotonated phosphonic group (Ca1–O 2.34 Å) and with the OH belonging to the alcoholic functionality (Ca1–O 2.41 Å). The other phosphonic group points farther away from the surface, establishing two *intra*-molecular H-bonds with the first phosphonic group (2.01 Å and 1.67 Å). The calculated BE of 286 kJ mol⁻¹ is definitely lower than for the previous case.

Model of Fig. 6c is aimed to study the interaction of AA with two Ca ions. By docking the AA towards the Ca1 and Ca3 surface ions it resulted in two rather short Ca–O contacts (2.28 Å and 2.35 Å, respectively) without proton transfer. Many H-bonds occurred at the surface (1.66, 1.56 and 1.37 Å, Fig. 6c), whereas a H-bond arises between the acidic phosphonic group and the NH₂ group of a replicated AA

molecule in a close cell (1.51 Å). The presence of two strong interactions between the phosphonic groups and the Ca ions accounts for a BE value of 385 kJ mol⁻¹, much larger than the two previous cases. We estimated the deformation energies of this model as no reaction occurred: the surface requires 54 kJ mol⁻¹ to be deformed from its original structure (δE_S) whereas AA needs, instead, 267 kJ mol⁻¹ for the geometrical deformation from its original conformation (ΔE_M). This is consistent with the previous assumption: the molecule needs energy to be unfolded to interact properly with the surface. The conformational energy cost is partially regained from the lateral interactions between adsorbates ($\Delta E_L = -147$ kJ mol⁻¹; this value becomes -109 when correcting for the BSSE). Then, the BE* (free of the deformation energies) is very large (559 kJ mol⁻¹). When correcting for the BSSE, the BE*^C value decreases to 413 kJ mol⁻¹, while the BE^C to 201 kJ mol⁻¹ (BSSE 48%). The relevance of the lateral interaction has also been checked by running a single point energy calculation on a 2 × 2 × 1 supercell with only one AA molecule per unit cell in the same geometry of the 1 × 1 × 1 model. In this case the lateral interactions are negligible and the resulting total adsorption energy amounts to -253 kJ mol⁻¹. This value is in excellent agreement with -237 kJ mol⁻¹ resulting from the 1 × 1 × 1 calculation, once the lateral interactions were removed and the deformation energy was properly taken into account (we are referring here to values not corrected for the BSSE as what matters is the internal comparison).

The three geometries presented are consistent with the previous simulation by Robinson *et al.*²⁸ (molecular mechanics, GAFF force field), in which the phosphonic groups pointed towards the most exposed calcium ion. Nevertheless, their energy is much lower than ours, because they accounted for the dielectric constant of the solvent, which reduces the electrostatic interactions. We also checked these results with a full reoptimization of the PBE structures at the B3LYP level. The corresponding BE are 322, 276 and 202 kJ mol⁻¹ (the latter BSSE corrected) for models of Fig. 6a–c on the HA(001), respectively, in excellent agreement with the PBE values. Further details are provided by Table S1 in the ESI.†

Interaction with the (010)WR surface. Only one model of the interaction of AA with the (010)WR surface was simulated (Fig. 7).

During the optimization one acidic proton of the phosphonic group was transferred to the NH₂ group of an AA adsorbed in a neighbour cell, which remains bound *via* a short H-bond (1.58 Å), while a second proton transfer occurs from one phosphonate group towards a surface oxygen atom (H-bond, 1.41 Å). A web of H-bonds arises towards surface oxygen atoms (1.74, 1.82, 1.74 and 1.90 Å) and only one Ca–O interaction is established (2.42 Å). The two H atoms originated from water dissociation interact with the adsorbed molecule through H-bonds (1.52 Å for the POH group, 2.07 Å for the OH). The BE of 402 kJ mol⁻¹ shows again the (010)WR surface to be more reactive than the (001) of HA, despite being already reacted with water.^{5,56} This result is also compatible with the studies by Bigi *et al.*^{29,30} They found that composite AA–HA nanocrystals display definitely smaller dimensions than HA nanocrystals together with a columnar crystalline habit along the [001] direction, which agrees with the

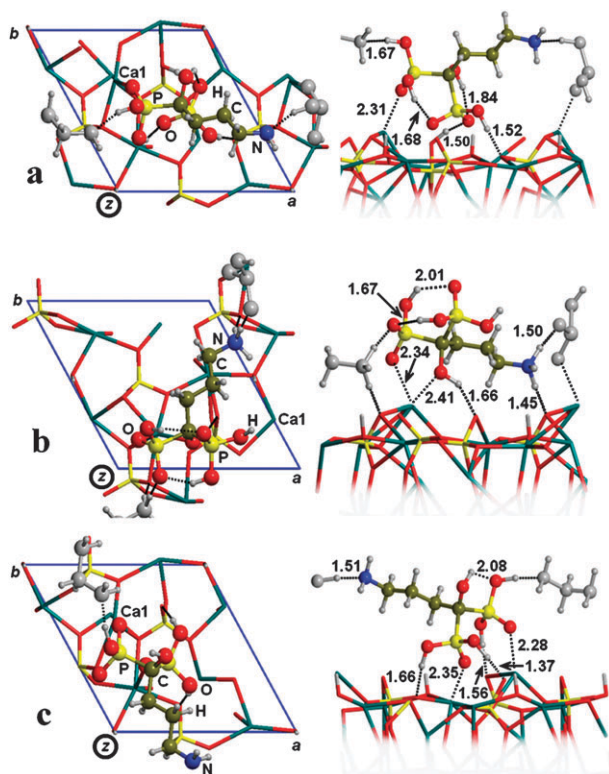


Fig. 6 AA on the HA (001) surface: top and local views of the three models. Bond lengths in Å. H-bonds and Ca–O_S as dashed lines.

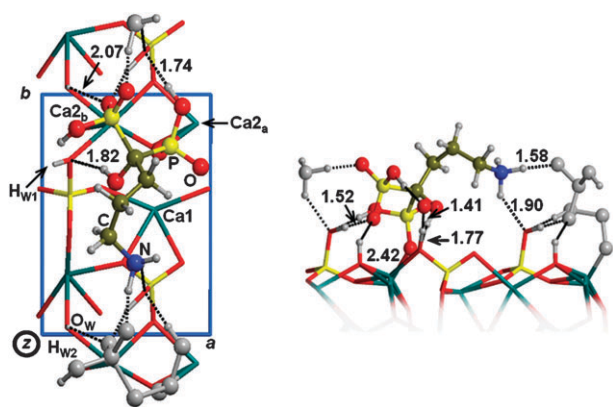


Fig. 7 AA on the HA (010)WR surface: top and local views of the considered model. Bond lengths in Å. H-bonds and Ca–O_s as dashed lines.

higher interaction of AA with the (010) surface than with the (001) one. As for the HA(001), the B3LYP full reoptimization gives a BE of 379 kJ mol⁻¹, slightly smaller than the PBE one (see Table S1 in the ESI†).

3.2 Theoretical infrared spectra

In order to give a new insight into the adsorption phenomena occurring at the two considered HA surfaces, we computed the PBE harmonic vibrational frequencies of the most significant cases of FA and AA interacting with the HA surfaces.

3.2.1 Infrared frequencies of FA adsorbed on HA surfaces.

Fig. 8 shows the absorbance infrared (IR) spectra (3600–500 cm⁻¹) of FA, formate, FA_O4, FA_Ca1, Ca3 and FA_(010) using data from Table 3.

All spectra were rescaled to match the PBE C=O stretching frequency of the free FA of 1817 cm⁻¹ (see Fig. 8, band *b*) with the experimental frequency⁶⁵ of 1740 cm⁻¹ (scaling factor of 0.96). All peaks in Fig. 8 were assigned by the potential energy distribution analysis, provided within CRYSTAL06. Peak *a* (Fig. 8) represents the C–H stretching, *b* the C=O stretching, *c* the H–C–O bending, *d* the H–O–C bending, *e* the C–O stretching, *f* the out of plane H–C–O bending, *g* the out of plane H–O–C bending, *h* the O–C–O bending and *j* the O–H stretching. Peak *k* is the outcome of the dissociative process of FA at the HA surfaces connected to the OH stretching, which will be examined later on.

Our simulated FA and formate gas-phase spectra agree reasonably with previous experimental and theoretical studies.^{49–51,53,54} Here we describe the major features of the gas-phase formate spectrum since it does not have any previous experimental counterpart. Many IR peaks of FA spectrum undergo a bathochromic shift in the formate one (see Fig. 8). Peak *a* (stretching C–H, $\Delta\nu = -712$ cm⁻¹), peaks *b* and *e*, well separated in the C_s FA, degenerate in the C_{2v} formate, giving two new modes, assigned to the asymmetric and symmetric C–O stretching (peaks *b_{asym}* and *b_{sym}*, Fig. 8). From now on, all comparisons of the C=O stretching of our four models will be addressed to peaks *b_{asym}* in formate. Peak *b* in FA is slightly bathochromically shifted in formate ($\Delta\nu = -55$ cm⁻¹). The

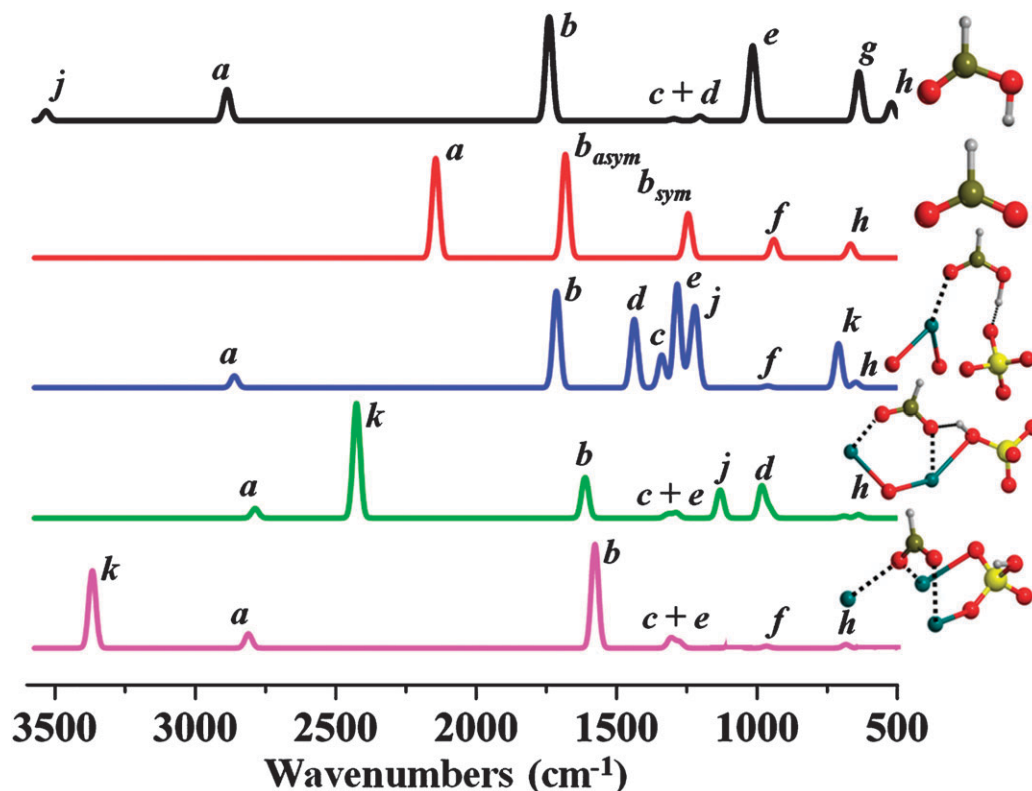


Fig. 8 Absorbance IR spectra (from top to bottom) of FA (gas-phase), formate, FA_O4, FA_Ca1, Ca3, FA_(010) (see model structures in Fig. 3–5, respectively). Original PBE harmonic frequencies were rescaled by 0.96 (see text for details) to ease the comparison with the experimental spectra (see Fig. 10). All peaks were represented by Lorentzian peaks of 30 cm⁻¹ bandwidth.

Table 3 Wavenumbers (ν , cm^{-1}) and hydrogen bond distances (HB, Å) of the most relevant stretching frequencies of FA molecule (both free and in interaction with the HA (001) and the (010)WR surfaces)

Modes	HCOOH	HCOO ⁻	FA_O4		FA_Ca1,Ca3		FA_(010)	
	ν	ν	ν	HB	ν	HB	ν	HB
<i>a</i>	2838	2126	2813	/	2742	/	2765	/
<i>b</i>	1740	1684	1715	/	1617	/	1584	/
<i>e</i>	1046	1684	1303	/	1308	/	1313	/
<i>j</i>	3456	/	1242	1.24	1157	1.53 ^a	/	/
<i>k</i>	/	/	754	1.19	2397	1.04	3298	0.99

^a Hydrogen atom belongs to the HA surface.

absence of the acid proton in formate causes a hypsochromic shift of the O–C–O bending ($\Delta\nu = +140 \text{ cm}^{-1}$, see peak *h* Fig. 8) as well as the outcropping of the H–C–O out of plane bending (*f*).

A first glance at the peak positions in Fig. 8 shows that model FA_O4 is similar to FA whereas cases FA_Ca1,Ca3 and FA_(010) to formate. Regarding the comparison of the adsorption models with the gas-phase FA and formate, two varieties of modes can be recognized. First of all, those IR modes modulated by the magnitude of FA–HA surfaces interaction: the O_{FA}–H_{FA} (*j*, Fig. 8) and the H_{FA}–O_S (*k*) stretching modes. These involve all the atoms of FA engaged directly in the interaction with the HA surface atoms (*e.g.* the acid hydrogen H_{FA}, the O_{FA} and the O_S, Fig. 3–5). The large bathochromic shift of the O–H_{FA} stretching (*j*) in FA_O4 ($\Delta\nu = -2320 \text{ cm}^{-1}$) indicates the strong contact of FA with the HA (001) surface. This was found even larger than the model FA_Ca1,Ca3 ($\Delta\nu = -2304 \text{ cm}^{-1}$), where the acid hydrogen is partially transferred to the surface (Fig. 4). In FA_Ca1,Ca3 and FA_(010) a new peak appears, attributed to the H_{FA}–O_S stretching (*k*, Fig. 8), which in the last model replaces thoroughly the O–H_{FA} (*j*) stretching, no longer observable.

Modes *b*, *c*, *d*, *e*, *f* and *h* (Fig. 8) outlined a sort of “pattern” of FA adsorbed on the HA surfaces. The majority of these (*c*, *d*, *e*, *f* and *h*) show very weak intensities and, hence, they will not be regarded as the main topic of our discussion. Such generalization is consistent with what expected in a real experiment, where feeble IR modes are likely to be mixed up either with the background or with the instrumental noise.

The very intense C=O stretching mode (*b*, Fig. 8) was found reliant on the way as FA interacts with the Ca ions of the HA surfaces. Models such as FA_Ca1,Ca3 and FA_010 (see Fig. 3, 4 and 5), where FA turns into formate, have their peak *b* close to the *b*_{asym} of the formate. Conversely in FA_O4 (Fig. 4), the C=O stretching remains similar to that of free-FA, as FA does not dissociate once adsorbed on the (001) surface of HA. This is further emphasized by the position of peak *e* (C–O stretching, Fig. 8), very similar to that in formic acid. On the other hand, partial or full dissociation of the acid hydrogen of FA on HA influenced the C=O mode to be similar to either free-FA or free-formate. Less visible IR modes, such as *c*, *d*, *f* and *h* (Fig. 8), experience an overall hypsochromic-shift from either FA or formate spectra.

3.2.2 Infrared frequencies of AA adsorbed on HA surfaces.

Fig. 9 shows the calculated infrared (IR) spectra of AA for the

free molecule and when adsorbed on the (001) and (010)WR surfaces, focusing on the 1500–3700 cm^{-1} region. The spectrum of the free AA was computed for the most stable conformation shown in Fig. 1. For the (001) case, only the most stable model (Fig. 6c) is discussed here. Table 4 reports the main stretching frequencies together with the relative H-bond distances (when present) to facilitate their interpretation.

The C–H stretching modes (ν_{CH}) fall always around 3000 cm^{-1} as these modes are not involved in any significant interaction with the surface.

For the free AA molecule, the stretching mode of the alcoholic group ($\nu_{\text{OH-alc}}$) falls at a very high frequency as it is free of H-bonds (see Fig. 1). This mode experiences weak bathochromic shifts upon adsorption, as it is involved on an *intra*-molecular H-bond when adsorbed on the (001) (2.08 Å, see Table 4 and Fig. 6c) and on a weak H-bond with the surfaces OH (1.82 Å, see Table 4 and Fig. 7) for adsorption on the (010)WR.

Three out of four PO–H groups in the AA free molecule are H-bonded and one is free (see Fig. 1 and Table 3). The computed PO–H stretching modes (*a*, *b*, *c* and *d*) resulted at well separated frequencies, the *a* mode being that of the free PO–H (its frequency is indeed the highest among the four PO–H ones). All the other PO–H frequencies undergo bathochromic shift depending on the H-bond strength. For the free AA, Table 4 shows a good correlation between PO–H frequency and H-bond length (see also Fig. 1), as band *b/c* are due to the longest/shortest PO–H···OH bonds, and band *d* to the shortest PO–H···NH₂ H-bond (see Fig. 1, 9 and Table 4). The lowest NH stretching frequency (3320 cm^{-1} , Table 3) falls very close to the *b* band for the free AA molecule resulting in an almost overlapped peak.

When AA interacts with the (001) surface, the following changes occur for the PO–H group of bands (see Fig. 6c): (i) all *a*, *b*, *c*, *d* are bathochromically shifted, as all PO–H groups are now involved in strong H-bond either with the HA surface (*a*, *b*, and *d* bands) or with the NH₂ group of AA adsorbed in the neighbour cell (*c* band). Both the stretching ν_{NH} and the bending δ_{HNH} modes remain unperturbed in the (001) spectrum compared to the free AA one as the interactions involving the NH₂ moiety are very similar for both cases (see Fig. 1 and 9 and Table 4).

The scenario changes dramatically when AA is adsorbed on the (010)WR surface (see Fig. 7) as proton transfer occurs between AA adsorbed on neighbour cells as well as towards the surface (*vide supra*). The OH belonging to the alcoholic group ($\nu_{\text{OH-alc}}$) are weakly perturbed as a rather long H-bond is established with the surface (1.82 Å, Fig. 7 and Table 4). The stretching and bending associated to the NH₂ moiety are strongly affected as this group becomes protonated due to the adsorption process. Among the PO–H modes, *c* and *d* are now due to the stretching of O–H groups belonging to the surface as a result of the proton transfer process.

3.3 Experimental study of the FA–HA interaction

As a preliminary remark, it is noteworthy to report that previous high resolution TEM investigations⁶⁶ revealed that HA nanoparticles employed for the experimental part of this

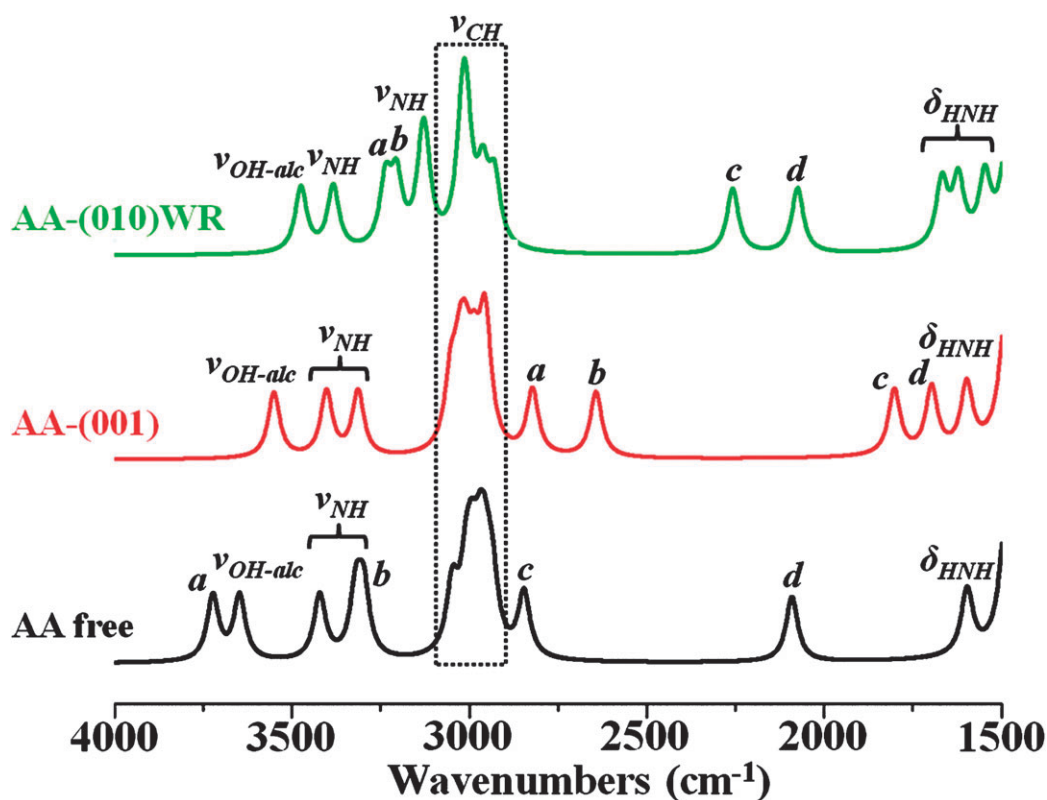


Fig. 9 Absorbance IR spectra (from bottom to top) of: (bottom) AA gas-phase (Fig. 1), (middle) AA on the HA (001) surface (Fig. 6c), (top) AA on the HA (010)WR surface (Fig. 7). All peaks were represented by Lorentzian peaks of 30 cm^{-1} bandwidth.

Table 4 Wavenumbers (ν , cm^{-1}) and hydrogen bond distances (HB, Å) of the most relevant stretching frequency of AA molecule (both free and in interaction with the HA (001) and the (010)WR surfaces)

Modes	AA free		AA-(001)		AA-(010)WR	
	ν	HB	ν	HB	ν	HB
<i>a</i>	3723	/	2822	1.66	3286	1.74
<i>b</i>	3298	1.90	2643	1.56	3205	1.77
<i>c</i>	2846	1.64	1802	1.51	2258 ^a	1.58 ^a
<i>d</i>	2091	1.52	1697	1.37	2075 ^a	1.41 ^a
$\nu_{\text{OH-alc}}$	3648	/	3551	2.08	3475	1.82
ν_{NH}	3422	/	3403	/	3384	/
ν_{NH}	3320	/	3314	/	3133	1.90

^a Hydrogen atom belongs to the HA surface.

study exhibited a platelet like morphology, with dimensions (length \times width \times thickness) of *ca.* $40\text{--}100 \times 40\text{--}100 \times 5\text{--}10\text{ nm}$, where the more extended surface planes should be of the (010) type, while the others appeared of the (100) and (001) types. In addition, different and more complex terminations occurred at the boundary among different surface planes, but they represented a minor fraction of the surface habitus. Thus, the material employed appeared as a reasonable experimental counterpart for the surface models considered for the modelling part.

Fig. 10 shows the $1800\text{--}1500\text{ cm}^{-1}$ range of spectra of FA adsorbed on the nano hydroxyapatite powder pre-outgassed at 433 K, to remove most part (*ca.* 85%) of water molecules initially coordinated to surface Ca ions.^{2,66}

Original spectra were recorded over the whole range of transparency of the HA self-supporting pellet ($4000\text{--}1250\text{ cm}^{-1}$).

However, the presence of bulk and surface carbonate species, producing a multi-components patterns in the $1500\text{--}1350\text{ cm}^{-1}$ range, hydroxyl and hydrogen phosphate groups, responsible for a broad signal spread over the $3500\text{--}2200\text{ cm}^{-1}$ range (see ESI[†], Fig. S1), rendered less effective the extraction of the signals due to adsorbed FA molecules in other spectral domains. In particular, components related to surface CO_3^{2-} , OH^- and POH underwent some modification after FA adsorption (partial displacement, modification of the interfacial refraction index and/or dipolar environment), resulting in the appearance of negative/sigmoidal features in the spectral profiles obtained after subtraction of the spectrum of the bare HA as background.

Initially, a small dose of FA vapour ($P_{\text{FA}} < 0.01\text{ mbar}$) was admitted onto the HA sample, producing a weak band at 1695 cm^{-1} and a more intense complex signal with maximum at 1593 cm^{-1} , broad and asymmetric on the high frequency side (Fig. 10A, curve a). As the contact time went on, such (two) absorptions exhibited an opposite behaviour. The higher frequency band became progressively weaker, shifting at 1690 cm^{-1} , whilst the other signal exhibited a significant increase in intensity, accompanied by some re-shaping, appearing finally narrower and less asymmetric (Fig. 10A, b–f). As the band at 1695 cm^{-1} appeared quite close in position to the $\nu\text{C}=\text{O}$ band observed for liquid FA (dotted line in Fig. 10A), such a spectral evolution should monitor the transformation, through an activated process, of FA molecules initially physisorbed into adsorbed species more strongly interacting with the surface sites.

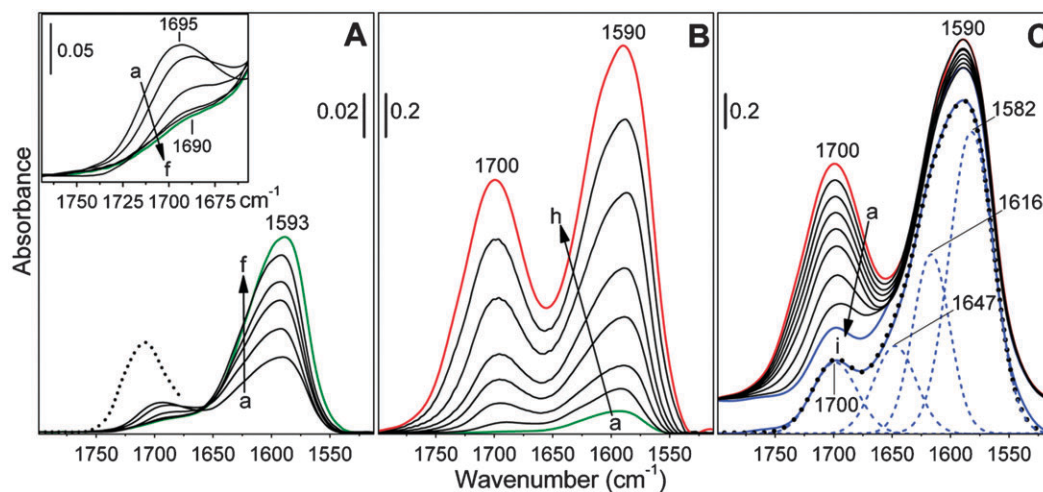


Fig. 10 IR spectra of formic acid (FA) adsorbed on hydroxyapatite (pre-outgassed at 433 K) through the vapour phase. Section A: (a) admission of a small dose of FA vapour (<0.01 mbar), and (b–f) subsequent spectral evolution for increasing contact time, up to 40 min. Dotted line: part of the IR spectrum of liquid HCOOH (thin film). Inset: zoomed view of the 1850 – 1650 cm^{-1} region. Section B: final spectra obtained at the end of the evolution occurring during the contact time with increasing pressure of FA (in the sense of the lettering), up to 1 mbar. Curve a is the same spectrum that curve f in section A (note the different scale). Section C: effect of the out-gassing of FA vapour at beam temperature (*ca.* 323 K), from (a) 1 mbar (the same spectrum that curve a in section B) to (i) direct pumping for 20 min. For the sake of clarity, a copy of spectrum i, blue curve, was plotted downshifted along the Y-axis, and over-imposed to the components obtained by de-convolution (dashed line) and the total spectrum resulting from their addition (dotted black line).

Subsequently, increasing doses of FA vapour were admitted onto the HA sample, up to a $P_{\text{FA}} = 1$ mbar, waiting for the accomplishment of the spectral evolution at each step. For the sake of simplicity, only the final spectral profiles are reported in Fig. 10B (note that the scale is changed with respect to panel A), resulting in the progressive growth of both components, finally located at 1700 and 1590 cm^{-1} , the high frequency one exhibiting a partial recovery in relative intensity with respect to the other. Noticeably, the band at 1700 cm^{-1} appeared quite close in position to the $\nu\text{C}=\text{O}$ band observed for liquid FA (dotted line in Fig. 10A), and this was the only component still increasing in intensity by contacting the sample with higher pressures of FA vapour (not shown), indicating the achievement of the saturation of surface sites able to adsorb FA.

Finally, P_{FA} was progressively decreased and then the sample was out-gassed under dynamic vacuum at beam temperature (*ca.* 323 K). As a consequence, a significant decrease in intensity of the 1700 cm^{-1} band occurred, while the 1590 cm^{-1} one appeared more stable (Fig. 10C).

Spectrum (i) in panel C was then assigned to species left irreversibly adsorbed on the HA surface that were considered as the experimental moiety to be compared with the results of the quantum mechanical modelling. A de-convolution of such spectral profile was carried out, and the best fitting was obtained by considering four components (Fig. 10C, bottom part, dotted curves). Noticeably, sub-bands at 1700 , 1616 and 1582 cm^{-1} are in really good agreement with frequencies calculated for FA₀₄ (1714 cm^{-1}), for FA_{Ca1,Ca3} (1617 cm^{-1}) and for FA-(010)WR species (1583 cm^{-1}), respectively (see peaks *b* in Fig. 8). As for these latter, the fact that the spectral evolution observed as the contact time went by (see Fig. 10A) resulted in a preferential increase of the lower frequency component of the 1593 cm^{-1} peak at the

expenses of the 1695 cm^{-1} band, indicated that the deprotonation of initially physisorbed FA molecules, producing formate species, is an activated process.

The component at 1647 cm^{-1} has no correspondence in the computed set of frequencies. Its presence can be reasonably related to the richness of different sites occurring on the surfaces of the experimental HA sample, not accounted for the ideal surface models adopted in the simulation. The location of such component suggests that it can be due to FA molecules adsorbed in a protonated form.

D. Summary and conclusions

The adsorption of FA and AA on the HA (001) and on water reacted (010)RW surfaces were simulated within the DFT using the PBE functional and Gaussian basis set as encoded in the CRYSTAL06 code. Adsorption of gas-phase FA on HA surface was also investigated experimentally through FT-IR spectroscopy experiments. Despite previous modelling studies from our group which adopted the B3LYP functional, PBE was selected as it is about three times quicker than the hybrid one, a fact which matters as we intend to simulate hydroxyapatite based systems of amorphous nature, as the Hench's bioglass⁶⁷ in the near future. Comparison between PBE and B3LYP for the adsorption of AA indeed showed a very good internal consistency between the two functionals.

The PBE results for the two surfaces and the FA and AA molecules were found in good agreement with previous experimental and/or theoretical studies. We modeled several adsorption cases, following as a guideline the electrostatic complementarity between the electrostatic potential of the molecules and surfaces. FA was found taking on two distinct behaviours, depending on the HA surface. On the one hand, FA can be molecularly adsorbed: this is the case of the (001)

surface, with binding energies values of about 190 kJ mol^{-1} . On the other hand, FA can dissociate on HA surfaces: this happens for the (010)WR model, where FA strongly interacts as a formate ion (BE value of 250 kJ mol^{-1}). We experienced just one case of FA dissociated on the (001) HA surface, however its BE remains lower than the other models about this surface. We calculated harmonic frequencies for the relevant adsorption models of FA on HA, which fit accurately the C=O zone ($1750\text{--}1550 \text{ cm}^{-1}$) of the experimental spectra recorded by us. As a rule of thumb, our simulations as well as FT-IR spectra show that FA binds strongly to the surface Ca cations, which is a helpful clue as how these ions can be potentially removed from the surface, triggering the HA dissolution.

The binding energy for AA adsorption spans the 280 to 400 kJ mol^{-1} range. In the majority of cases, the mechanism of the AA adsorption is dissociative, with proton transfer towards either the HA basic sites or the NH_2 moiety of AA molecule adsorbed on the neighbour cell. This feature was not found in previous molecular-mechanics calculations since they considered the zwitterionic form of the molecule.

Nevertheless, *ab initio* and molecular-mechanics calculations confirm the high affinity of the phosphonic groups for the Ca ions of the surfaces. The highest binding energy was for the interaction with the (010)WR surface, explaining why the composite HA/AA nanocrystals grow along the *c*-axis, dominated by the (001) surface. At variance with the FA case, the acid(OH)/basic(NH_2) functionalities of the AA molecule allow for multiple interactions, *i.e.* with the HA surfaces and *via* lateral interactions with strong H-bonds between OH groups of one molecule and the NH_2 moiety of its first AA images adsorbed on neighbour cells. This causes a uniform coverage at the HA surfaces by AA resulting in a "surface protector" against dissolution.

Acknowledgements

Some of the largest calculations of this work have been supported by generous allowance of computer time from Barcelona Supercomputing Centre (Projects: BCV-2008-2-0013; BCV-2008-3-0006: Simulation of peptide folding induced by inorganic materials) and CINECA computing centre. Part of this work has also been supported by the Italian Ministry MIUR (Project COFIN-2006, Prot. 2006032335 Interface phenomena in silica-based nanostructured biocompatible materials contacted with biological systems) and by Regione Piemonte-Italy (Project CIPE-2004, Nanotechnologies and Nanosciences Nanostructured materials biocompatible for biomedical applications). Y.S. is recipient of a PhD fellowship from Compagnia di San Paolo. The CRYSTAL team headed by R. Dovesi (Dip. Chimica IFM, University of Torino) and Mr Ruslan Khatipov are acknowledged for providing support on the CRYSTAL06 code and collection of IR spectra, respectively. The authors are obliged to Prof. N. Roveri (University of Bologna) for having provided nano-HA powder and to Prof. S. Coluccia (University of Torino) for fruitful discussion.

Notes and references

1 H. Suda, M. Yashima, M. Kakihana and M. Yoshimura, *J. Phys. Chem.*, 1995, **99**, 6752–6754.

- 2 L. Bertinetti, A. Tampieri, E. Landi, C. Ducati, P. A. Midgley, S. Coluccia and G. Martra, *J. Phys. Chem. C*, 2006, **111**, 4027–4035.
- 3 M. Corno, C. Busco, B. Civalleri and P. Ugliengo, *Phys. Chem. Chem. Phys.*, 2006, **8**, 2464–2472.
- 4 M. Corno, A. Rimola, V. Bolis and P. Ugliengo, *Phys. Chem. Chem. Phys.*, 2010, **12**, 6309–6329.
- 5 M. Corno, C. Busco, V. Bolis, S. Tosoni and P. Ugliengo, *Langmuir*, 2009, **25**, 2188–2198.
- 6 A. Rimola, M. Corno, C. M. Zicovich-Wilson and P. Ugliengo, *J. Am. Chem. Soc.*, 2008, **130**, 16181–16183.
- 7 R. Astala and M. J. Stott, *Phys. Rev. B: Condens. Matter Mater. Phys.*, 2008, **78**, 075427.
- 8 A. Rimola, M. Corno, C. M. Zicovich-Wilson and P. Ugliengo, *Phys. Chem. Chem. Phys.*, 2009, **11**, 9005–9007.
- 9 D. Zhan and O. Hochrein, *Phys. Chem. Phys.*, 2003, **5**, 4004.
- 10 S. M. Vratsanos and I. D. Mandel, *J. Dent. Res.*, 1982, **61**, 465–468.
- 11 H. C. Margolis and E. C. Moreno, *J. Dent. Res.*, 1990, **69**, 302–302.
- 12 H. C. Margolis and E. C. Moreno, *Calcif. Tissue Int.*, 1992, **50**, 137–143.
- 13 H. C. Margolis and E. C. Moreno, *Crit. Rev. Oral Biol. Med.*, 1994, **5**, 1–25.
- 14 H. C. Margolis, Y. P. Zhang, C. Y. Lee, R. L. Kent and E. C. Moreno, *J. Dent. Res.*, 1999, **78**, 1326–1335.
- 15 M. Yoshioka, Y. Yoshida, S. Inoue, P. Lambrechts, G. Vanherle, Y. Nomura, M. Okazaki, H. Shintani and B. Van Meerbeek, *J. Biomed. Mater. Res.*, 2002, **59**, 56–62.
- 16 Y. Yoshida, B. Van Meerbeek, Y. Nakayama, J. Snauwaert, L. Hellemans, P. Lambrechts, G. Vanherle and K. Wakasa, *J. Dent. Res.*, 2000, **79**, 709–714.
- 17 N. H. de Leeuw, J. R. Bowe and J. A. L. Rabone, *Faraday Discuss.*, 2007, **134**, 195–214.
- 18 Z. F. Chen, B. X. Huang, H. B. Pan and B. W. Darvell, *Cryst. Growth Des.*, 2009, **9**, 2816–2820.
- 19 L. J. Wang, R. K. Tang, T. Bonstein, C. A. Orme, P. J. Bush and G. H. Nancollas, *J. Phys. Chem. B*, 2005, **109**, 999–1005.
- 20 F. P. Coxon, K. Thompson and M. J. Rogers, *Curr. Opin. Pharmacol.*, 2006, **6**, 307–312.
- 21 C. T. Leu, E. Luegmayr, L. P. Freedman, G. A. Rodan and A. A. Reszka, *Bone*, 2006, **38**, 628–636.
- 22 G. H. Nancollas, R. Tang, R. J. Phipps, Z. Hennem, S. Gulde and W. Wu, *Bone*, 2006, **38**, 617–627.
- 23 J. Fabad, *Pharm. Sci.*, 2006, **31**, 31–42.
- 24 Y. Zhang, R. Cao, F. Yin, M. P. Hudock, R.-T. Guo, K. Krysiak, S. Mukherjee, Y.-G. Gao, H. Robinson, Y. Song, J. H. No, K. Bergen, A. Leon, L. Cass, A. Goddard, T.-K. Chang, F.-Y. Lin, E. Van Beek, S. Papapoulos, A. H.-J. Wang, T. Kubo, M. Ochi, D. Mukkamala and E. Oldfield, *J. Am. Chem. Soc.*, 2009, **131**, 5153–5162.
- 25 A. G. Porras, S. D. Holland and B. J. Gertz, *Clin. Pharmacokinet.*, 1999, **36**, 315–328.
- 26 S. C. L. M. Cremers, G. C. Pillai and S. E. Papapoulos, *Clin. Pharmacokinet.*, 2005, **44**, 551–570.
- 27 S. Mukherjee, C. Huang, F. Guerra, K. Wang and E. Oldfield, *J. Am. Chem. Soc.*, 2009, **131**, 8374–8375.
- 28 J. Robinson, I. Cukrowski and M. H. Marques, *J. Mol. Struct.*, 2006, **825**, 134–142.
- 29 E. Boanini, M. Gazzano, K. Rubini and A. Bigi, *Adv. Mater.*, 2007, **19**, 2499–2502.
- 30 E. Boanini, P. Torricelli, M. Gazzano, R. Giardino and A. Bigi, *Biomaterials*, 2008, **29**, 790–796.
- 31 R. Dovesi, V. R. Saunders, C. Roetti, R. Orlando, C. M. Zicovich-Wilson, F. Pascale, B. Civalleri, K. Doll, N. M. Harrison, I. J. Bush, P. D'Arco and M. Llunell, *CRYSTAL06, User's Manual*, 2008.
- 32 C. Pisani, R. Dovesi and C. Roetti, *Lecture Notes in Chemistry* **48**, Springer, Berlin, Heidelberg, New York, 1988, p. 193.
- 33 W. Kohn and L. J. Sham, *Phys. Rev.*, 1965, **140**, 1133–1138.
- 34 P. Hohenberg and W. Kohn, *Phys. Rev.*, 1964, **136**, 864–871.
- 35 P. Ugliengo, G. Borzani and D. Viterbo, *Z. Kristallogr.*, 1988, **185**, 712.
- 36 P. Ugliengo, D. Viterbo and G. Chiari, *Z. Kristallogr.*, 1993, **207**, 9.
- 37 W. Humphrey, A. Dalke and K. Schulten, *J. Mol. Graphics*, 1996, **14**, 33–38.
- 38 R. Dovesi, M. Causà, R. Orlando and C. Roetti, *J. Chem. Phys.*, 1990, **92**, 7402–7411.
- 39 M. Catti, R. Dovesi, A. Pavese and V. R. Saunders, *J. Phys.: Condens. Matter*, 1991, **3**, 4151–4164.

- 40 A. Schafer, H. Horn and R. Ahlrichs, *J. Chem. Phys.*, 1992, **97**, 2571.
- 41 J. P. Perdew, B. Burke and M. Ernzerhof, *Phys. Rev. Lett.*, 1996, **77**, 3865–3868.
- 42 C. G. Broyden, *IMA J. Appl. Math.*, 1970, **6**, 76–90.
- 43 R. Fletcher, *Comput. J.*, 1970, **13**, 317–322.
- 44 D. Goldfarb, *Math. Comput.*, 1970, **24**, 23–26.
- 45 D. F. Shanno, *Math. Comput.*, 1970, **24**, 647–656.
- 46 S. F. Boys and F. Bernardi, *Mol. Phys.*, 1970, **19**, 553–556.
- 47 A. S. Coolidge, *J. Am. Chem. Soc.*, 1928, **50**, 2166–2178.
- 48 E. Bjarnov and W. H. Hocking, *Z. Naturforsch., A: Phys., Phys. Chem., Kosmophys.*, 1978, **33**, 610–618.
- 49 G. Buemi, *J. Phys. Org. Chem.*, 2009, **22**, 933–947.
- 50 J. C. Dobrowolski, M. H. Jamroz, J. K. Kazimirski, K. Bajdor, M. A. Borowiak and R. Larsson, *J. Mol. Struct.*, 1999, **483**, 183–187.
- 51 K. Marushkevich, L. Khriachtchev, J. Lundell and M. Räsänen, *J. Am. Chem. Soc.*, 2006, **128**, 12060–12061.
- 52 S. Tosoni, C. Tuma, J. Sauer, B. Civalleri and P. Ugliengo, *J. Phys. Chem. B*, 2007, **127**, 154102–154111.
- 53 H. B. Pan and B. W. Darvell, *Arch. Oral Biol.*, 2007, **52**, 618–624.
- 54 J. Y. Park and D. E. Woon, *Astrophys. J.*, 2006, **648**, 1285–1290.
- 55 P. K. Weiner, R. Langridge, J. M. Blaney, R. Schaeffer and P. A. Kollman, *Proc. Natl. Acad. Sci. U. S. A.*, 1982, **79**, 709–713.
- 56 M. Corno, R. Orlando, B. Civalleri and P. Ugliengo, *Eur. J. Mineral.*, 2007, **19**, 757–767.
- 57 P. Rulis, H. Z. Yao, L. Z. Ouyang and W. Y. Ching, *Phys. Rev. B: Condens. Matter Mater. Phys.*, 2007, **76**, 15.
- 58 M. R. T. Filgueiras, D. Mkhonto and N. H. de Leeuw, *J. Cryst. Growth*, 2006, **294**, 60–68.
- 59 S. A. M. Tofail, D. Haverty, K. T. Stanton and J. B. McMonagle, *Ferroelectrics*, 2005, **319**, 117–123.
- 60 A. C. Legon and D. J. Millen, *Discuss. Faraday Soc.*, 1982, **73**, 71.
- 61 A. C. Legon, *Chem. Soc. Rev.*, 1990, **19**, 197.
- 62 C. A. Hunter, *Angew. Chem., Int. Ed.*, 2004, **43**, 5310–5324.
- 63 P. Ugliengo, F. Pascale, M. Merawa, P. Labeguerie, S. Tosoni and R. Dovesi, *J. Phys. Chem. B*, 2004, **108**, 13632–13637.
- 64 D. Fernández, D. Vega and A. Goeta, *Acta Crystallogr. Sect. C: Cryst. Struct. Commun.*, 2003, **59**, m543–m545.
- 65 G. Herzberg, *Molecular Spectra and Molecular Structure*, D. Van Nostrand Co, 1945.
- 66 L. Bertinetti, Y. Sakhno, A. Tampieri, M. Iafisco, N. Roveri and G. Martra, *J. Phys. Chem. C*, 2010, **114**, 16640–16648.
- 67 L. L. Hench, R. J. Splinter, W. C. Allen and T. K. Greenlee, *J. Biomed. Mater. Res. Symp.*, 1971, **2**, 117–141.